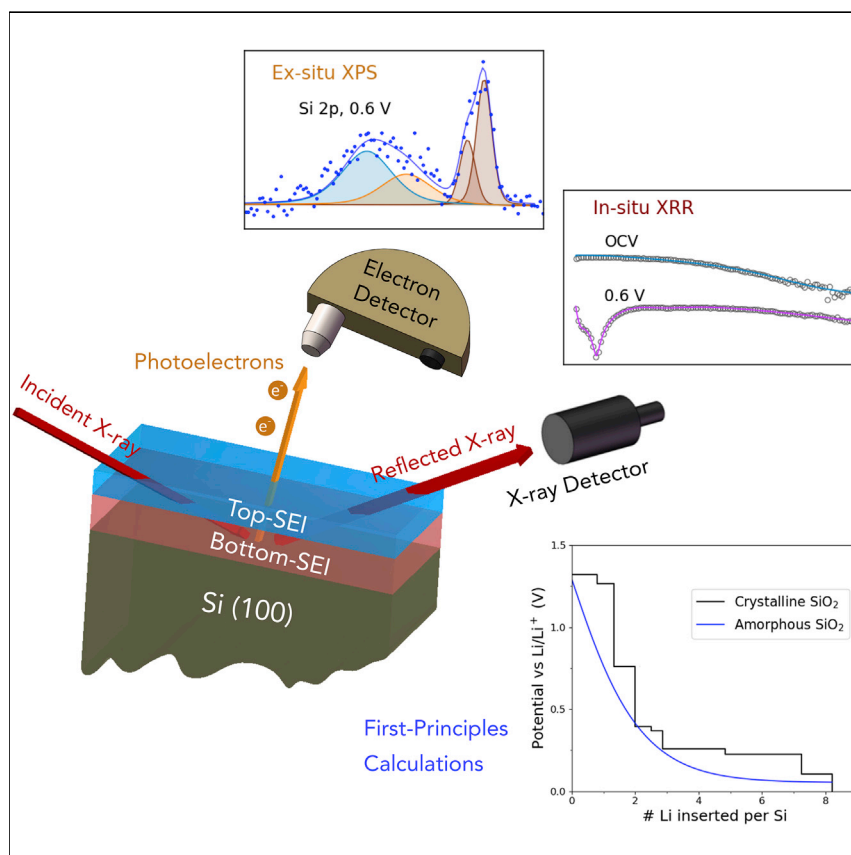


Article

Solid Electrolyte Interphase on Native Oxide-Terminated Silicon Anodes for Li-Ion Batteries



The solid electrolyte interphase (SEI) is a passivation layer naturally formed on battery electrodes. It protects electrodes and electrolytes from degradation and dictates charging time capabilities and lifetime. Despite its importance, it remains a poorly understood battery component. This study provides novel insights into the formation, morphology, and composition of the SEI on Si anodes through a multi-modal approach. The findings show a layered SEI and the ion and electron conductivities, as well as their relation to performance, are discussed.

Chuntian Cao, Iwnetim Iwnetu Abate, Eric Sivonxay, ..., Kristin A. Persson, Hans-Georg Steinrück, Michael F. Toney

hgs@slac.stanford.edu (H.-G.S.)
mftoney@slac.stanford.edu (M.F.T.)

HIGHLIGHTS

Multi-property study of the structure and composition of the SEI

Potential-dependent growth of two well-defined inorganic SEI layers on Si/SiO₂ anode

Unraveling of Li⁺ and e⁻ transport properties through the SEI

Article

Solid Electrolyte Interphase on Native Oxide-Terminated Silicon Anodes for Li-Ion Batteries

Chuntian Cao,^{1,2} Iwnetim Iwnetu Abate,^{1,2,3} Eric Sivonxay,⁴ Badri Shyam,¹ Chunjing Jia,³ Brian Moritz,³ Thomas P. Devereaux,³ Kristin A. Persson,⁴ Hans-Georg Steinrück,^{1,5,*} and Michael F. Toney^{1,*}

SUMMARY

To shed light on the formation process and structure of the solid electrolyte interphase (SEI) layer on native oxide-terminated silicon wafer anodes from a carbonate-based electrolyte (LP30), we combined *in situ* synchrotron X-ray reflectivity, linear sweep voltammetry, *ex situ* X-ray photoelectron spectroscopy, and first principles calculations from the Materials Project. We present *in situ* sub-nanometer resolution structural insights and compositional information of the SEI, as well as predicted equilibrium phase stability. Combining these findings, we observe two well-defined inorganic SEI layers next to the Si anode—a bottom-SEI layer (adjacent to the electrode) formed via the lithiation of the native oxide, and a top-SEI layer mainly consisting of the electrolyte decomposition product LiF. Our study provides novel mechanistic insights into the SEI growth process on Si, and we discuss several important implications regarding ion and electron transport through the SEI layer.

INTRODUCTION

Finding novel high-energy density energy storage devices is essential for the electrification of transportation.^{1,2} Silicon (Si) anode-based Li-ion batteries (LIBs) offer huge promise in this regard by providing a high theoretical capacity of 3,579 mAh/g, ten times higher than commercially utilized graphite-metal oxide-based LIBs.^{3–6} However, the widespread utilization of Si-based LIBs is still limited because of cyclability issues associated with large-volume expansion and uncontrolled solid electrolyte interphase (SEI) growth. The alloying process of Si with up to four Li atoms per Si atom,⁷ as compared to the fundamentally different intercalation mechanism of one Li atom per six carbon (C) atoms in graphite,⁸ leads to a volume expansion of up to 400%.^{9,10} In addition to the resultant pulverization of Si particles and concomitant electrical and mechanical disconnection,^{11–13} which leads to capacity fading, this massive volume change induces mechanical instability and cracking and subsequent reformation of the SEI.¹⁴

The SEI is a thin interfacial layer formed on anode surfaces as a result of electrolyte decomposition at low potentials outside the electrolyte's electrochemical stability window, which occurs during battery operation.¹⁵ As a result of its electrically insulating as well as solvent and counterion diffusion-prohibiting nature, its formation and growth is in principle self-limiting. The ideal SEI thus forms a protective film that allows for facile Li-ion transport and prevents further electrolyte decomposition. Therefore, associated initial capacity loss due to the initial SEI formation can be tolerated. However, in the case of mechanical failure of the SEI upon Si anode

Context & Scale

Despite the electronic revolution initiated by lithium-ion batteries (LIBs) three decades ago, one aspect of these energy storage devices still puzzles researchers. This is the solid electrolyte interphase (SEI) that forms on electrodes because LIBs operate outside the electrolyte stability window and can effectively passivate the electrode. Experimentally, the SEI is challenging to study with the desired atomic resolution as it is buried at the electrolyte-electrode interface.

In this article, we provide fresh insights into the nature and transport properties of the SEI, via a multi-property combined experimental and simulation approach utilizing well-defined model systems. We unraveled the structure and composition, as well as the formation mechanism of the SEI on silicon anodes. Our findings are discussed with regard to understanding possible SEI-induced bottlenecks in LIBs and the relevance for their optimization.

volume expansion, new unpassivated anode surfaces are created. These experience further electrolyte exposure, and decomposition on the Si surface continues during continued cycling. This leads to continued capacity loss since Li ions are consumed during its formation, and the corresponding inhomogeneity can result in higher electrical resistance and slower Li-ion transfer kinetics.¹⁶

In recent years, a large number of research groups investigated SEI properties on oxide-terminated Si electrode surfaces.¹⁷ For example, the morphology of the SEI on Si nanowires was reported, by combining X-ray photoelectron spectroscopy (XPS) and scanning electron microscopy (SEM), to be voltage dependent, appearing thicker at low potential, and experiencing cracking and partial dissolution during delithiation.^{18–25} Veith et al. performed *ex situ* XPS, showing that the SEI forms electrochemically above 0.6 V, continues to grow during SiO₂ and Si lithiation, and contains carboxylates, ethers or esters, and fluorides in equal concentrations with LiF and Li₂CO₃.^{19,20} Moreover, several XPS and NMR studies argue that the lithiation of SiO₂ involves a conversion reaction (i.e., SiO₂ + 4Li → Si + 2Li₂O) and the formation of Li₄SiO₄^{21–23} or Li₂Si₂O₅.²⁴ These lithiation products, which are considered part of the SEI, have a strong impact on the SEI's properties and, therefore, affect the cyclability of the battery electrode. For example, Li₄SiO₄ has been reported to exhibit low ionic conductivities,²⁶ which may limit ion diffusion through the SEI during charging and discharging of LIBs, and therefore prohibits fast charging rates.

We previously reported *in situ* XRR studies probing the real-time galvanostatic lithiation and delithiation of crystalline Si (001), providing a mechanistic atomic-scale 3-stage lithiation model.^{27,28} Our results further suggested that the integrated amount of inorganic SEI layer increases during lithiation and decreases during delithiation, resembling a “breathing” behavior; the inorganic SEI layer thickness varies between 40 and 70 Å. Additionally, a low electron density layer was found at the SEI|lithiated Si interface during the delithiation process, suggesting kinetically limited ion transport within the SEI, which is speculated to be one of the origins of battery's internal resistance.²⁸

Despite these efforts and its performance dictating nature, including most prominently electrochemical reversibility and cell chemistry kinetics,²⁹ the SEI remains “the most important and the least understood” part of LIBs.³⁰ This includes the SEI formation processes, the SEI composition and thickness, as well as the associated structure-function relationship to the electrochemical cycling performance. Poor understanding of the SEI has created difficulties in the development of mechanistic insights into many physical and chemical properties of the SEI such as ion transport, which is a crucially important factor in battery performance.³¹ Computational modeling performed to investigate the properties of the SEI (e.g., Li-ion diffusivity, stability, and electrolyte reduction pathways) is also limited because of the lack of knowledge of the SEI's composition and its evolution. It is generally understood that the SEI consists of an outer more organic part at the SEI-electrolyte interface and an inner, electrode-adjacent, more inorganic part.^{32–34} The outer part is the “organic SEI” and mainly consists of organic reaction products, including semicarbonates and polymers or oligomers; the inner part is the “inorganic SEI” and is mainly composed of inorganic Li compounds such as LiF and Li₂O.³¹ Because these solid-solid and solid-liquid interfaces are buried interfaces and the layers are thin (approaching 1 nm), they are experimentally challenging to characterize, particularly *in situ*, and with the desired atomic or molecular resolution. Other factors that contribute to the limited understanding of the SEI originate in its complexity, including morphology, trace presence, and large variety of anodes as well as the electrolytes and additives used in studying its formation, growth, and structure.^{35–38}

¹SSRL Materials Science Division, SLAC National Accelerator Laboratory, Menlo Park, CA 94025, USA

²Department of Materials Science and Engineering, Stanford University, Stanford, CA 94305, USA

³Stanford Institute for Materials and Energy Sciences, SLAC National Accelerator Laboratory and Stanford University, Menlo Park, CA 94025, USA

⁴Department of Materials Science and Engineering, University of California, Berkeley, Berkeley, CA 94720, USA

⁵Lead Contact

*Correspondence: hgs@slac.stanford.edu (H.-G.S.), mftoney@slac.stanford.edu (M.F.T.)

<https://doi.org/10.1016/j.joule.2018.12.013>

To overcome these issues, we sought out a reductionist approach, in which we utilized a simple and well-defined model system for our study of SEI formation, i.e., single crystalline, atomically smooth native oxide-terminated Si (001) wafers. Accordingly, we studied the SEI under well-defined electrochemical conditions, focusing on determining the SEI's nucleation and growth, as well as its thickness and composition in order to develop a detailed model describing the potential-dependent evolution of the SEI. Toward this end, we have combined *in situ* X-ray reflectivity (XRR), linear sweep voltammetry (LSV), *ex situ* X-ray photoelectron spectroscopy (XPS), and first principles calculations (FPC) results obtained from the Materials Project (MP)³⁹ to determine the SEI's composition, thickness, and its evolution as a function of voltage. Thereby, we developed a better understanding of the SEI growth and formation mechanism on native oxide-terminated single crystalline Si anodes, in addition to gaining insights into the SEI's functionality such as ion transport.

Through our multi-property study of the SEI, we show the formation of two well-defined sub-layers within the inorganic SEI. A "bottom-SEI" layer at the Si-SEI junction, which is a result of the lithiation of the native oxide initiated at 0.7 V, contains mostly Li_xSiO_y with some Li_xSi_y . The electrolyte electrochemically decomposes at 0.6 V into inorganic products, including LiF, forming the "top-SEI" layer at the bottom-SEI|electrolyte interface. Our study provides a detailed understanding of the effects of native oxide on SEI growth, and we discuss the relevance for battery performance as well as provide quantitative insights into capacity losses into inorganic and organic SEI. We envision that our methodology will open a new path toward quantitative SEI research that can be widely applied to study SEI formation in other electrolyte-electrode model systems. We also anticipate that our chemical and structural understanding of the SEI can lead to new approaches for the design of superior protection layers, e.g., in terms of ion transport properties.

RESULTS

In Situ X-Ray Reflectivity

In situ XRR experiments were performed in half-cell configuration with a native oxide-terminated (001)-Si wafer as the working electrode, Li metal as the counter and reference electrode, and a 1:1 wt % ethylene carbonate (EC):dimethyl carbonate (DMC) electrolyte containing 1 M LiPF_6 (LP30). Details of the experimental setup can be found in the [Experimental Procedures](#). During our *in situ* XRR measurements, the Si wafer working electrode potential was galvanostatically decreased at $50 \mu\text{A}/\text{cm}^2$ to several target voltages and held there until two consecutive XRR datasets were identical within the experimental accuracy. The current at this stage dropped below 30% of the initial value; a typical decay time was tens of minutes. Two potential-hold XRR experiments were performed: (A) high-potential sequence, in which the cell was galvanostatically cycled from open circuit voltage (OCV) (typically 2.3–3.3 V) at $50 \mu\text{A}/\text{cm}^2$ to 1, 0.9, 0.8, 0.7, and 0.6 V, and held at these voltages, and (B) low-potential sequence, in which the cell was galvanostatically cycled at $50 \mu\text{A}/\text{cm}^2$ from OCV to 0.6, 0.5, 0.4, 0.3, 0.2, and 0.1 V, and held there. Under these conditions, it is reasonable to assume that steady-state conditions were reached, i.e., no kinetic limitations were present. This allowed us to relate each electrode potential to SEI properties. In each experiment, XRR data was collected through both the galvanostatic discharge and the potential hold process with a time resolution of approximately 5 min. Notice that XRR is only sensitive to the inorganic part of the SEI because of the lack of scattering contrast between the organic SEI and the electrolyte^{27,28} (the electron densities are nearly identical).

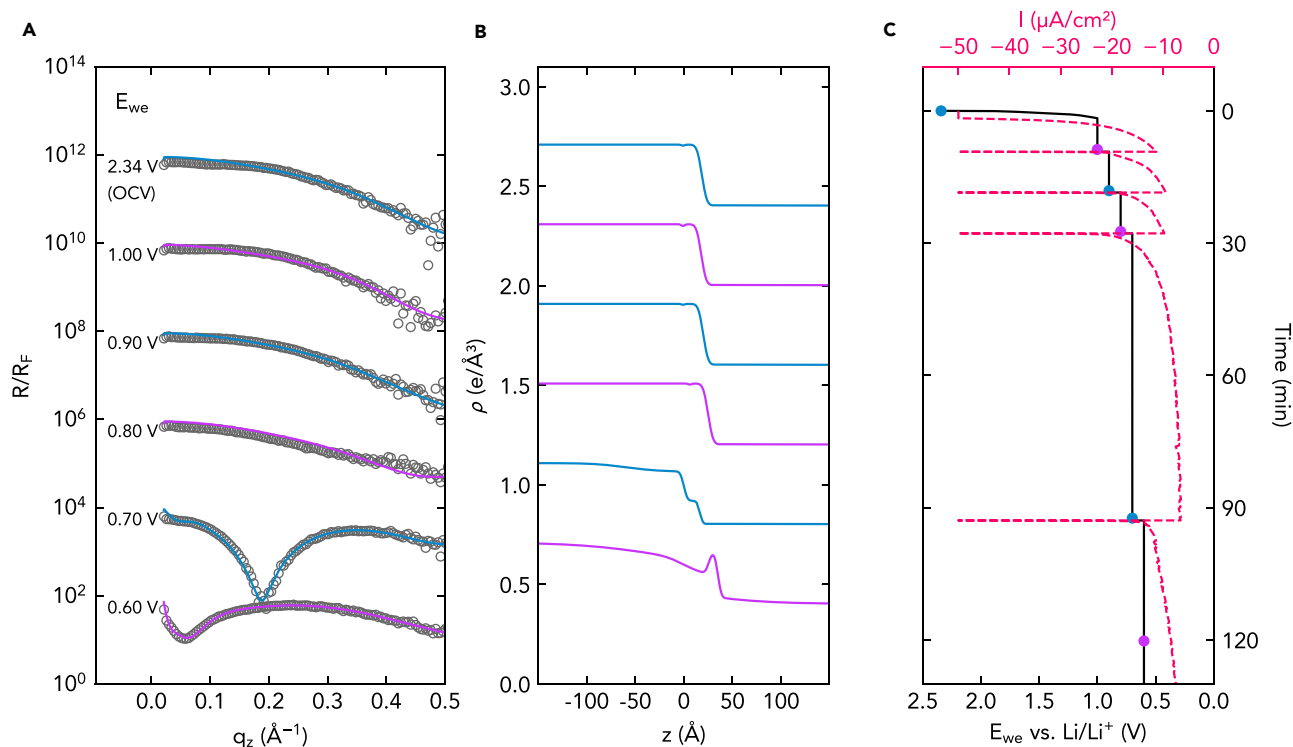


Figure 1. In Situ XRR Results from High-Potential-Sequence Experiments

(A) Measured, Fresnel-normalized (R/R_F) XRR data (symbols) and model fits (solid lines). The corresponding voltages are annotated on the left side of each scan.

(B) Fit-derived electron density profiles (EDPs). $z = 0$ is arbitrarily set to the Si-SEI interface.

(C) Electrochemistry in which the black solid line represents the voltage profile and the dashed red curve represents the corresponding current response.

The curves in (A) and (B) are vertically shifted for clarity.

Our *in situ* XRR results are illustrated in Figure 1 (high-potential sequence) and Figure 2 (low-potential sequence). Figures 1A and 2A show the scattering vector (q_z) dependence of the measured Fresnel normalized XRR (markers) and model fits (lines) to the electron density profiles (EDPs) shown in Figures 1B and 2B as a function of distance from the Si-SEI interface. Figures 1C and 2C depict the corresponding applied voltage and current response of the Si working electrode as a function of time. For simplicity, only the steady-state XRR curves at the end of each potential hold process are shown here. The intermediate XRR curves during which the potential was constant, in which the evolution of the XRR can be seen, are shown in Figures S1 and S2.

High-Potential Sequence

We first discuss the high-potential sequence, where the potential of the Si working electrode was held at 1, 0.9, 0.8, 0.7, and 0.6 V. The topmost XRR curve was measured at OCV and was fitted using the electrolyte|native SiO_2 |Si model.⁴⁰ The roughness of the native oxide was determined to be about 4 Å. The XRR curves at voltages 1, 0.9, and 0.8 V exhibited no significant differences from those at OCV and were thus fit to the same EDP model. At 0.7 V, a large dip appears at $q_z \approx 0.2 \text{ \AA}^{-1}$, indicating the formation of a new interfacial layer with a thickness of approximately $\pi/q_{z_{\text{min}}} \approx 16 \text{ \AA}$. This curve is well described by a model consisting of the bottom-SEI, initially lithiated Si and Si substrate. The initial- Li_xSi layer is formed by a small amount of Li that has diffused into bulk Si causing an average density drop

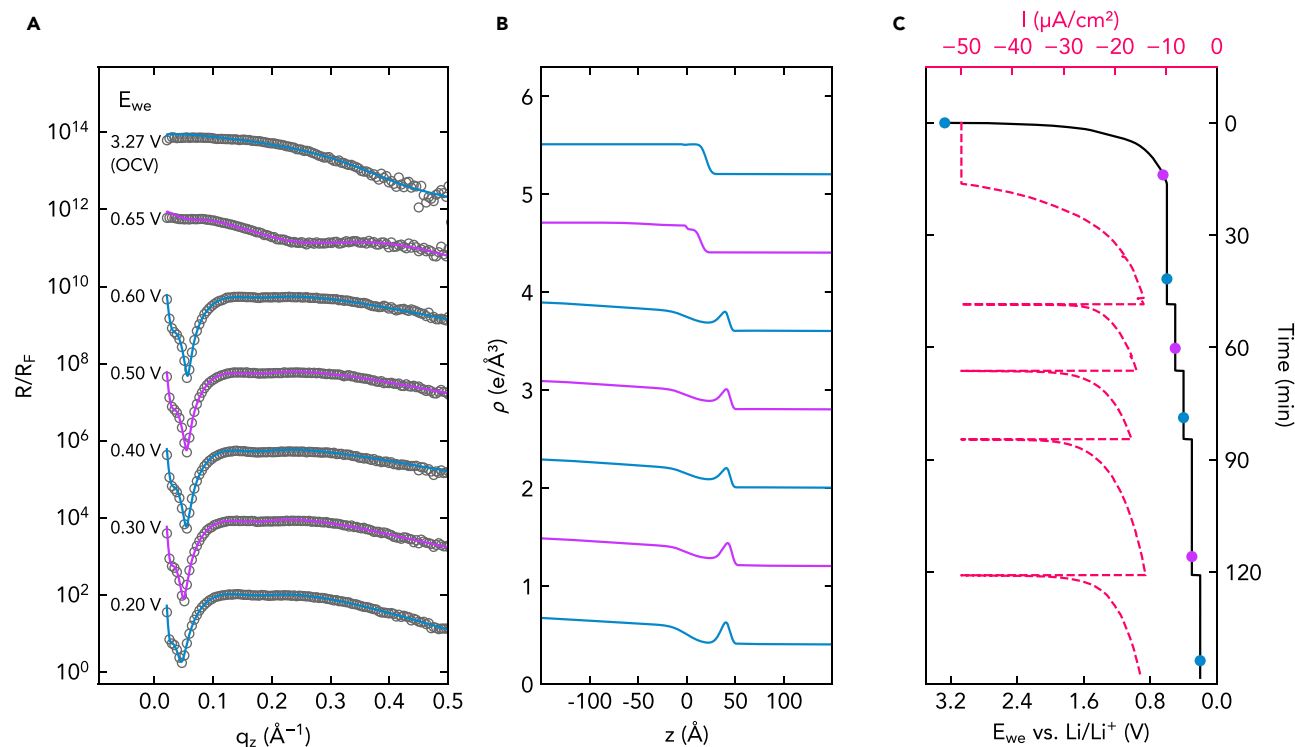


Figure 2. In Situ XRR Results from Low-Potential-Sequence Experiments

(A) Measured, Fresnel-normalized (R/R_F) XRR data (symbols) and model fits (solid lines). The voltage of each scan is annotated on the left side.

(B) Fit-derived electron density profiles (EDPs).

(C) Electrochemistry in which the black solid line represents the voltage profile and the dashed red curve represents the corresponding current response.

The curves in (A) and (B) are vertically shifted for clarity.

of $\sim 10\%$ ^{27,28} (a rationalization of this model is presented in the [Supplemental Information](#), Section 2). We refer to the observed SEI layer that is directly adjacent to the electrode as the “bottom-SEI” because a higher-density “top-SEI” layer forms on top of the bottom-SEI at lower potentials. The dip in the XRR curve becomes less pronounced at 0.6 V and shifts to a lower q_z value of $\approx 0.06 \text{\AA}^{-1}$, which corresponds to a total SEI thickness of $\sim 50 \text{\AA}$. The curve at 0.6 V is well fitted by three layers in addition to the Si substrate. Starting from the electrolyte, these are the top-SEI layer, the bottom-SEI layer, and the initial- Li_xSi layer. All fit-derived parameters are tabulated in [Table S1](#). The uncertainties were determined as described previously and are shown in [Supplemental Information](#), Section 3.^{27,41,42}

Low-Potential Sequence

The low-potential-sequence XRR experiment is summarized in [Figure 2](#). The OCV curve is similar to the one in [Figure 1](#) and was fitted using the same SiO_2/Si model. During the galvanostatic lithiation process from OCV to 0.6 V, the XRR curve at $\sim 0.65 \text{ V}$ exhibits a minimum at $q_z \sim 0.24 \text{\AA}^{-1}$, which is similar to the 0.7 V curve in the high-potential-sequence experiment. We noted that this cell was not held at 0.65 V but continued to discharge until 0.6 V was reached, at which potential a sharp minimum at $q_z \sim 0.055 \text{\AA}^{-1}$ appears. The position is similar to that found in the high-potential-sequence experiment at the same voltage, albeit of slightly different shape. This curve was fitted using the top-SEI/bottom-SEI/initial Li_xSi three-slab model. It is worth noting that we encountered similarly shaped XRR curve shapes in our previous reports^{27,28} at $\sim 0.3 \text{ V}$ during galvanostatic lithiation, which was

well described by the same 3-slab model. Previously, we tentatively assigned the corresponding layers to SEI, Li_xSi , and initial- Li_xSi , without compositional knowledge of either the Li_xSi layer or its evolution because of limited time resolution. Via the controlled potential experiments in combination with the XPS measurements reported here, we can now confidently assign the low-density region between the top-SEI and initial- Li_xSi to the bottom-SEI layer; the compositions of top- and bottom-SEI layers were studied via XPS and will be discussed below. At 0.5 V and 0.4 V, the changes in the XRR curves appear to be insignificant compared to 0.6 V, which is confirmed by the unchanged EDPs in Figure 2B. At 0.3 V, the minimum shifts from 0.055 \AA^{-1} to 0.051 \AA^{-1} with slightly increased amplitude implying that the SEI grows by about 5 \AA , while the electron density remains unchanged ($\sim 0.47 \text{ e/\AA}^3$). At 0.2 V, the minimum shifts further to a lower value of approximately 0.047 \AA^{-1} (further increase by about 5 \AA), indicating further SEI growth; the electron density decreases to $\sim 0.40 \text{ e/\AA}^3$. The EDPs (from 0.6 to 0.2 V) are overlapped in the Figure S3, for the sake of highlighting their differences.

X-Ray Reflectivity Findings

The SEI layer thickness and electron density from the high-potential and low-potential-sequence XRR experiments are quantitatively summarized in Figures 3A–3E, depicting the fit-derived parameters for the top- and bottom-SEI. These show that the bottom-SEI nucleates at 0.7 V, initially grows from 0.7 to 0.6 V, and then remains at a constant thickness but with decreasing density toward lower potentials down to 0.3 V. The top-SEI begins to grow at 0.6 V, with increasing thickness and density as the potential is lowered. At 0.2 V, the bottom-SEI layer becomes significantly lower in density, consistent with the formation of Li_2O . The final thicknesses at 0.2 V are approximately 7 \AA for the top-SEI layer and 38 \AA for the bottom-SEI layer. This 15 \AA (SiO_2) to 38 \AA (lithiated- SiO_2) thickness change is a 2.3 times expansion of the native oxide upon lithiation and agrees with our previous findings²⁷ as well as previous TEM imaging.⁴³ The roughnesses of the bottom- and top-SEI are found to be below 7 \AA , which appears reasonable under the assumption that the bottom-SEI grows on the atomically smooth native oxide and that the thin top-SEI layer grows conformally on top of the bottom-SEI. The higher-density value of top-SEI ($0.7\text{--}0.8 \text{ e/\AA}^3$) compared to the bottom-SEI ($0.4\text{--}0.5 \text{ e/\AA}^3$) indicates that these consist mainly of LiF (nominal density 0.74 e/\AA^3) and $\text{Li}_x\text{SiO}_y/\text{Li}_2\text{O}$ (nominal density $0.71/0.57 \text{ e/\AA}^3$), respectively. A lower density of the bottom-SEI than nominal values suggests some presence of lower-density species, such as Li_xSi , which is discussed in the Discussion section. This hypothesis is confirmed in the sections below, in which our XRR results will be discussed in context with our XPS results.

Linear Sweep Voltammetry

In order to relate our structural findings to electrochemical measurements, we performed LSV of an oxide-terminated Si wafer at 0.1 mV/s with the same half-cell configuration in a Teflon cone cell.^{44,45} This cell was utilized because it eliminates parasitic currents, only the active material (and inert Teflon) is in contact with the electrolyte, and it has a well-defined surface area (1.27 cm^2). This yields precision voltammetry. Parasitic currents are unavoidable in our *in situ* XRR electrochemical XRR cell.^{27,28} The LSV scan shows three reduction peaks located at 0.70, 0.56, and 0.23 V, agreeing well to the growth of the bottom-SEI at 0.7 V, the top-SEI at 0.6 V, and further evolution of the bottom-SEI at 0.2 V found in our XRR experiments. At voltages above 0.8 V, which is before the start of the 0.7 V peak, there is a small but non-zero current; the possible origins of this current are explained in the Supplemental Information, Section 6.3.

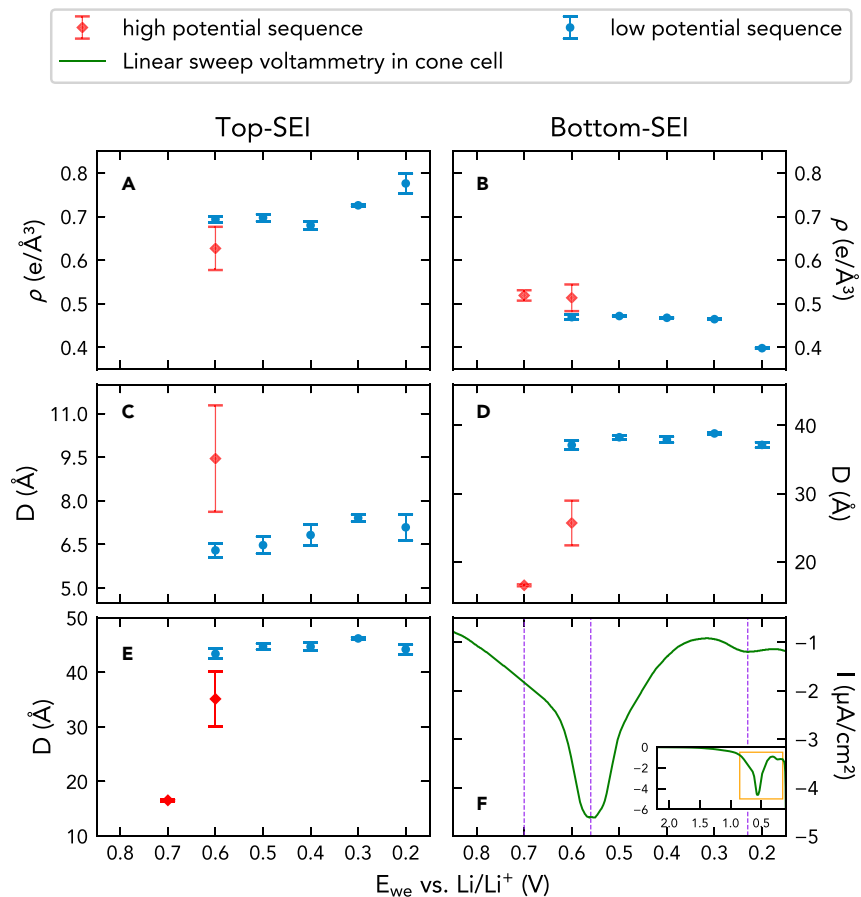


Figure 3. Best-Fit Results of XRR Datasets of High-Potential (Red Markers) and Low-Potential (Blue Markers) Sequence Experiments

(A) Electron density of the top-SEI layer.

(B) Electron density of the bottom-SEI layer.

(C) Thickness of the top-SEI layer.

(D) Thickness of the bottom-SEI layer.

(E) Total thickness, i.e., sum of thicknesses of the top- and bottom-SEI layers.

(F) Linear sweep voltammetry (LSV) from OCV (2.5 V) to 0.1 V at 0.1 mV/s using a Teflon cone cell.

The calculation method of the error bars in (A)–(E) is explained in the [Supplemental Information](#), Section 3. The inset of (F) shows the full LSV profile, and the orange rectangular region of the inset is magnified and shown in (F).

Ex Situ X-Ray Photoelectron Spectroscopy

Because XRR does not directly probe chemical composition, we performed complementary *ex situ* XPS measurements in order to gain information on the composition of the top- and bottom-SEI layers. [Figures 4A–4D](#) depict the XPS spectra and corresponding fits for Si 2p, O 1s, F 1s, and Li 1s for OCV and after 2 h voltage holds at 0.8, 0.7, 0.6, 0.3, and 0.2 V. The fitted peaks are colored with the following color coding: SiO₂ is blue, Li_xSiO_y is orange, Si is brown, Li₂O is red, LiPF₆ is green, and LiF is magenta. The C 1s and P 2p spectra are inconclusive and are shown in [Figure S5](#). The literature binding energies of all relevant compositions are tabulated in [Table S2](#). Our XPS findings are summarized in [Figure 5](#), in which the best-fit peak areas corresponding to Si, SiO₂, Li_xSiO_y, Li₂O, and LiF are depicted with the same color coding as in [Figure 4](#). We now discuss the evolution of the XPS spectra via qualitative assessment of [Figure 4](#) in combination with more quantitative assessment of [Figure 5](#).

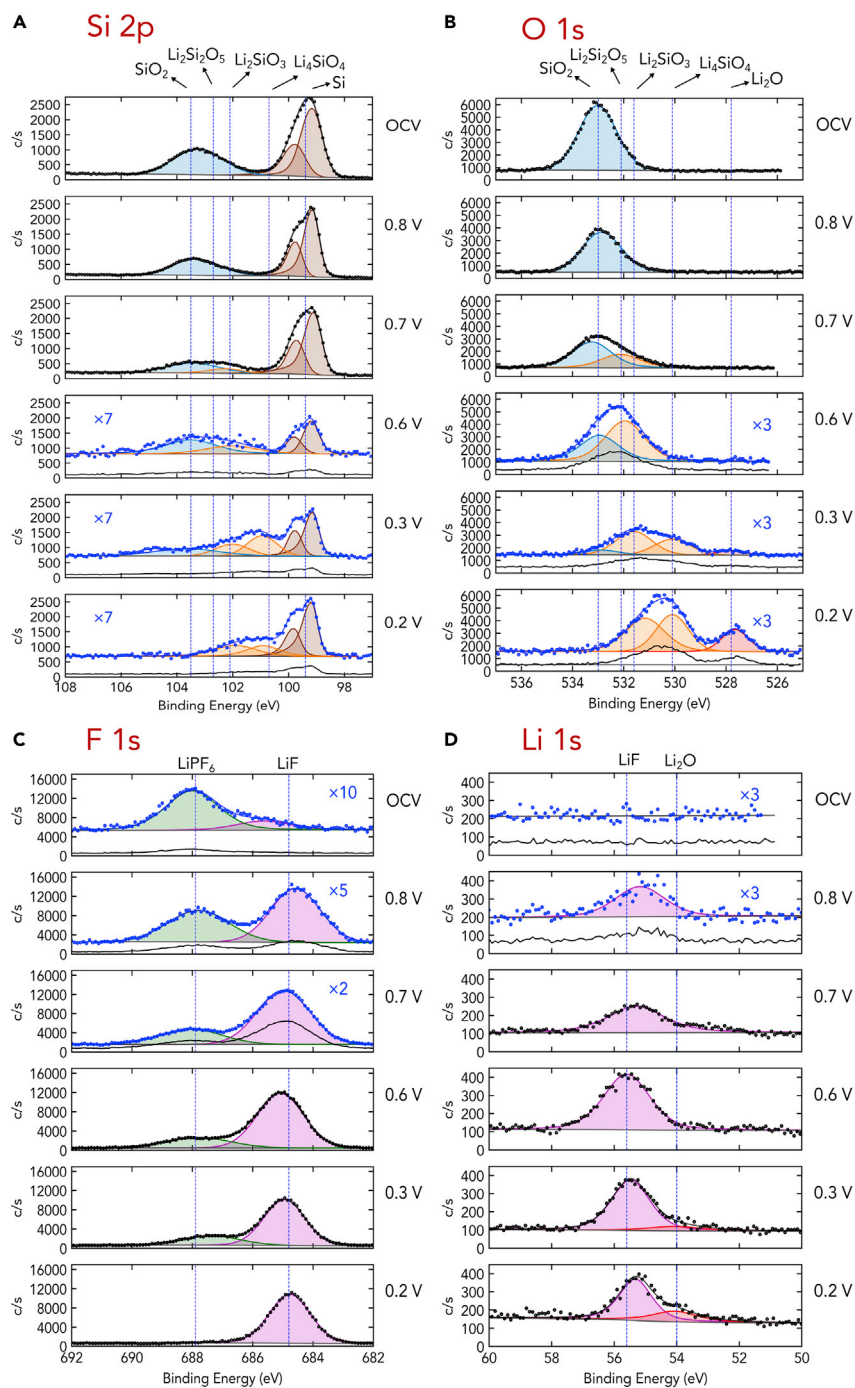


Figure 4. XPS Spectra of the Si 2p, O 1s, F 1s, and Li 1s Spectral Range

(A–D) Spectra of Si 2p (A), O 1s (B), F 1s (C), and Li 1s (D) generated in the XPS are shown. In each figure, the XPS results from samples at OCV and cycled to and held at 0.8, 0.7, 0.6, 0.3, and 0.2 V are shown. The vertical dashed lines indicate the characteristic binding energies (obtained from the literature) of the annotated compounds. The blue curves are multiplied by the numbers indicated in the respective panel for easier comparison.

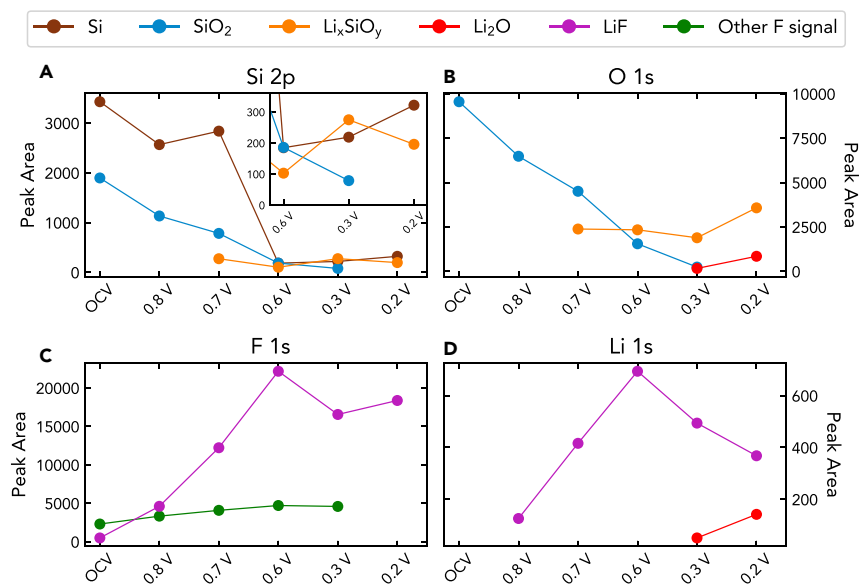


Figure 5. Voltage-Dependent XPS Fit-Derived Peak Areas Corresponding to Si 2p, O 1s, F 1s, and Li 1s Spectral Ranges

(A–D) XPS peaks corresponding to Si 2p (A), O 1s (B), F 1s (C), and Li 1s (D) spectral ranges from different compounds are indicated by different colors, as shown in the legend. The O 1s peak areas from Li_xSiO_y at 0.3 V and 0.2 V are calculated from the sum of the Li_xSiO_y peaks in Figure 4. The inset of (A) magnifies the Si 2p peak areas below 0.6 V.

OCV

0.8 V. The Si 2p spectra at OCV show peaks corresponding to bulk Si (99.4 eV) and SiO_2 (native oxide) (103.5 eV),⁴⁶ the O 1s spectra show the corresponding SiO_2 peak (533 eV).⁴⁷ The Si 2p and O 1s spectra at OCV and 0.8 V show minimal changes, which suggests that the native oxide layer remains intact, consistent with our XRR results. The small amount of Li and F present at the surface at 0.8 V is attributed to residual electrolyte even after DMC washing⁴⁸ and the formation of organic SEI, as well as possibly small amounts of electrolyte decomposition.^{49–51}

0.7 V. Reducing the potential from 0.8 to 0.7 V results in changes in all spectra. In particular, we observed increased intensity in the Si 2p and O 1s spectra in the lithium silicate (Li_xSiO_y) spectral range from 100.7 to 102.7 eV, and 530.1 to 532.1 eV, respectively, whereas both spectra still contain intensity corresponding to SiO_2 , although reduced in intensity. This indicates that the native oxide starts to be partially lithiated around 0.7 V, forming mostly Li_xSiO_y . We note that as a result of the weak intensity and the broad peaks seen in the XPS from Li_xSiO_y , we could not assign the peaks to specific Li_xSiO_y species. In addition to Li_xSiO_y , Si and lithium silicide (Li_xSi) are also SiO_2 lithiation products^{52–54} (also predicted by our first principles calculations). These products (and the initial LiSi_x) are not observed, which we believe is because of this being indistinguishable from bulk Si in the Si 2p spectrum for small x and resulting from lack of resolution and statistics.²²

0.6 V. Starting from 0.6 V, the peak intensities assigned to LiF ⁵⁵ in the Li 1s and F 1s spectra increase more than 4-fold compared to their respective intensities at 0.8 V, and more than 2-fold compared to 0.7 V. This suggests a substantial electrolyte decomposition reaction at 0.6 V forming an inorganic SEI layer containing largely LiF. The attenuation of the SiO_2 and Li_xSiO_y peaks in the Si 2p and O 1s indicates that electrolyte decomposition and LiF layer formation takes place on top of Li_xSiO_y .

Despite observing some LiF at 0.7 V, we conclude that the main contribution to LiF growth is centered on 0.6 V. This is based on a combination of XRR, XPS (Si and SiO₂ peaks are damped compared to 0.7 V), and LSV. We thus conclude that the bottom-SEI layer corresponds to lithiation of the native oxide, which starts at 0.7 V and the top-SEI layers is formed by electrolyte decomposition, with the main onset at 0.6 V. This is consistent with our LSV experiments, which show reduction peaks at 0.7 and 0.55 V as well as with our XRR results, which show the formation of a low-density interfacial layer (bottom-SEI) at 0.7 V and an additional higher-density layer on top (top-SEI) at 0.6 V. The top-SEI layer densities from XRR are consistent with this inorganic SEI layer containing mostly LiF, although we cannot exclude other SEI components such as lithium carbonates or lithium alkyl carbonates, especially in trace quantities. Other studies^{22,56} have indicated that Li₂CO₃ has formed at the end of lithiation or after one cycle, which may suggest that Li₂CO₃ either forms at lower potentials than we examined, or forms part of the organic SEI.

0.3 V. At 0.3 V, the peaks in the Si 2p and O 1s spectra corresponding to Li_xSiO_y shift to lower binding energies, indicating that Li_xSiO_y is further reduced toward a “fully lithiated” Li₄SiO₄. Furthermore, a peak at ~527.5 eV in the O 1s spectrum and a new peak at ~54 eV in the Li 1s spectrum appear. These were assigned to Li₂O, indicating the onset of Li₂O formation.^{51,57} The intensities in the Li_xSiO_y spectral range remain fairly unchanged, but the intensities in the SiO₂ range further decrease, although still residually present. We explain these phenomena by a concomitant further reduction of SiO₂ to Li_xSiO_y and the formation of Li₂O. The F 1s spectrum (LiF) shows no significant change.

0.2 V. At 0.2 V, the Li₂O peaks in the O 1s and Li 1s spectra become significantly stronger (about 3-threefold compared to 0.3 V). This is consistent with our XRR results, which shows significant changes only at 0.2 V (at 0.3 V, the amount of Li₂O is likely too small to observe), and the reduction peak in our LSV measurements at 0.23 V. Moreover, the decrease of the bottom-SEI electron density at 0.2 V can be explained by the presence of Li₂O. The Li_xSiO_y and SiO₂ intensities change insignificantly.

Our XPS measurements can be summarized into three main trends: (1) the initial formation of Li_xSiO_y starts at approximately 0.7 V, (2) the major contribution to the decomposition of the electrolyte is centered on 0.6 V and results in the formation of LiF on top of Li_xSiO_y, and (3) Li₂O is formed between 0.3 and 0.2 V. These observations are consistent with our XRR findings (Figures 3A–3E), which show the formation of a lower density bottom-SEI layer at 0.7 V, a higher density top-SEI layer at 0.6 V, and the modification of the bottom-SEI layer around 0.2 V. These observations are also consistent with our LSV measurements (Figures 3A–3F) showing reduction peaks at 0.7, 0.56, and 0.23 V. Our XPS results are in qualitative agreement with XPS studies in the literature^{22,58} but differ quantitatively because of different experimental and lithiation conditions. Specifically, our experiments were performed during the first cycle down to 0.2 V prior to full lithiation of the Si, and on Si single crystals. In contrast, the referenced studies include XPS measurements of Si particles within binders and conductive carbons performed after Si lithiation, i.e., after large-volume expansion associated with Si lithiation. This could explain the reported observation of significant amounts of lithium carbonates and lithium alkyl carbonates in these papers, in contrast to our work.

First Principles Calculations

FPC from the MP were utilized to further unravel the SiO₂ lithiation process using a thermodynamic approach with crystalline structures as a first approximation.⁵⁹

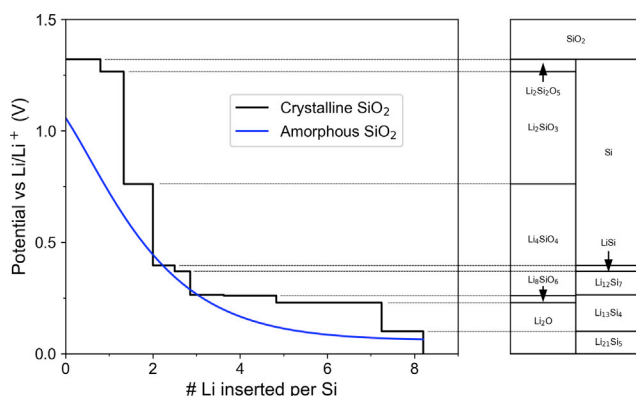


Figure 6. First Principles Calculations Derived Voltage Profiles

FPC results of the voltage profiles for amorphous (blue) and crystalline (black) SiO_2 as compared with calculated phase equilibria of crystalline SiO_2 upon lithiation constructed from the Materials Project.³⁹

Voltage profiles and phase equilibria of SiO_2 upon lithiation are the main findings of these calculations and are shown in Figure 6. Under thermodynamic equilibrium, the lithiation of the crystalline SiO_2 starts at 1.32 V, where SiO_2 is lithiated, forming $\text{Li}_2\text{Si}_2\text{O}_5$ and Si. With further decrease in the potential, there are multiple voltage plateaus corresponding to further lithiation of these products. For example, $\text{Li}_2\text{Si}_2\text{O}_5$ is reduced to Li_2SiO_3 at 1.27 V, which is stable between 1.27 V and 0.76 V. With decreasing potential, stable phases of Li_2SiO_3 , Li_4SiO_4 , and Li_8SiO_8 are predicted to form, followed by Li_2O formation below 0.25 V. Si is a reaction product starting at the beginning of SiO_2 lithiation at 1.32 V down to 0.4 V, but below this voltage, the product changes to Li-Si alloys.

As a more realistic model, using a “melt-and-quench” approach,^{60,61} amorphous analogs to a range of Li_xSiO_y compositions were constructed at different Li contents. Details of this approach are described in Supplemental Information Section 7. The amorphous potential profile in Figure 6 exhibits a similar shape as the crystalline one: the initial voltage is high (>1.2 V) and drops rapidly during the Li inserting into SiO_2 , during which Li-O bonds are formed at the expense of decreasing the number of Si-O bonds. Below 0.4 V, we observe the favorable formation of stable crystalline silicide phases corresponding to LiSi, $\text{Li}_{12}\text{Si}_7$, $\text{Li}_{13}\text{Si}_4$, and $\text{Li}_{21}\text{Si}_5$. Examination of the amorphous structures corroborates this trend, exhibiting local environments commensurate with Li_2O and Li_xSi domains as predicted by the crystalline phase equilibria depicted in Figure 6.

We then compared our computational results to our experimental data. In our XPS experiments, Li_xSiO_y was detected, with the corresponding Si 2p and O 1s peaks shifting to lower binding energies with decreasing potential. This indicates the formation of increasingly Li-rich silicates (see Figures 4A and 4B). Assigning the observed XPS peak positions to the characteristic Si 2p and O 1s binding energies of $\text{Li}_2\text{Si}_2\text{O}_5$, Li_2SiO_3 , and Li_4SiO_4 , we observe that $\text{Li}_2\text{Si}_2\text{O}_5$ and Li_2SiO_3 are present at a high potential (0.7 V), Li_2SiO_3 is the main contributor with decreasing potential, and Li_4SiO_4 is mostly present at a lower potential (0.2 V). The order of occurrence of these compounds as a function of potential is in accordance with the calculation results in Figure 6.

It is noteworthy that the simulations and experiments were not carried out under equivalent conditions. First, FPC assume thermodynamic equilibrium and do not

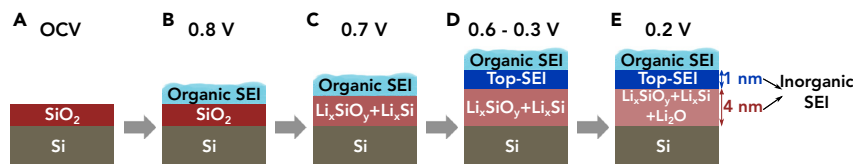


Figure 7. Schematic Illustration of the Proposed Potential-Dependent SEI Growth Mechanism on Native Oxide-Terminated Si Anodes

For the sake of simplicity, the electrolyte is omitted in this schematic.

(A) OCV, pristine native oxide (red) terminated Si (gray) substrate.

(B) 0.8 V, organic SEI has formed on the Si surface; native oxide layer has not reacted.

(C) 0.7 V, native oxide layer is lithiated forming the bottom-SEI containing Li_xSiO_y .

(D) 0.6 V, electrolyte decomposition forming the top-SEI layer containing inorganic reaction

products such as LiF; the bottom-SEI continues to lithiate. This status continues until 0.3 V.

(E) 0.2 V, Li_2O forms in the bottom-SEI. From 0.7 to 0.2 V, the initial- Li_xSi layer underneath the SEI is omitted for simplicity.

consider kinetics effects that can result in non-equilibrium reaction pathways and associated overpotentials. The SiO_2 is assumed to be bulk-like in the calculation. In our experiment, however, the native oxide is a thin film of ~ 1.5 nm thickness on bulk Si, exhibiting known structural and electronic differences from bulk SiO_2 .⁶² Additionally, the simulations are performed for $\text{SiO}_2\text{:Li}$, whereas bulk Si underlies the SiO_2 in the experiment, and we cannot rule out that this plays a role in the reduction of SiO_2 . These dissimilarities explain quantitative differences in the experiment and the simulation. For example, the Li_xSiO_y formation potentials predicted from FPC are higher than what we obtained from XRR, LSV, and XPS experiments. This is rationalized by the overpotential of the native oxide (because of its confined geometry), which can explain a significant deviation of the reaction potential from the FPC-predicted equilibrium potential. The second difference is that we do not observe evidence for the existence of Li_xSi in our XPS spectra at low voltages. While Si and Li_xSi are also predicted from calculation, and inevitable from stoichiometric constraints, this cannot be observed in XPS, because it is indistinguishable from the substrate (Si). Nevertheless, we note that the electron density of the bottom-SEI ($\sim 0.5 \text{ e}/\text{\AA}^3$) is smaller than the theoretical density of typical crystalline Li_xSiO_y ($\sim 0.7 \text{ e}/\text{\AA}^3$). This lower-density indicates that the bottom-SEI has low-density components, which could be due to the amorphous nature of Li_xSiO_y or the presence of a mixture of Li_xSi and Li_xSiO_y , or a combination of both. A possible explanation for the lack of Li_xSi signal in XPS is that the amount of x in Li_xSi is small, rendering a weak peak close to the substrate Si peak that cannot be resolved.

DISCUSSION

By combining *in situ* XRR, LSV, *ex situ* XPS, and FPC, we propose a detailed picture of the SEI formation process on Si anodes, which we illustrate schematically in Figure 7. For Si anodes terminated with their native oxide (Figure 7A, OCV), the organic SEI layer starts to form at above 1.5 V (Figure 7B, 0.8 V).^{63–65} The organic SEI cannot be detected by XRR because its electron density is too similar to that of the electrolyte.²⁷ Furthermore, we observed that a quantification/confirmation of organic SEI components by *ex situ* XPS is challenging, as a result of the DMC washing processes, during which organics species are likely to be washed off the substrates.^{19,29}

We show in the Supplemental Information, Section 6, that the organic SEI can comprise up to $\approx 6 \mu\text{Ah}/\text{cm}^2$, or up to several nm of thickness. No inorganic SEI is observed above 0.7 V, as significant changes in the XRR curves would be expected in this scenario. The native oxide begins to lithiate at 0.7 V (Figure 7C), forming Li_xSiO_y (exhibiting higher Li ratios at lower potentials), with side products

Si and Li_xSi . This layer was termed “bottom-SEI” layer. The composition was concluded from the combination of all techniques. Notice that the lithiation of SiO_2 due to charge neutrality and stoichiometric constraints necessarily also leads to the formation of Si and Li_xSi . While we do not observe a Li_xSi peak in either XPS or XRR, in particular the density values of the bottom-SEI suggests some presence of Li_xSi , in accordance with our FPC (below 0.4 V). Given trace amounts of Li_xSi , compared to bulk Si, and the fact that the Li_xSi peaks are close to bulk Si peaks, in particular at small x , we conclude that we cannot observe Li_xSi at low lithium contents in our XPS measurements. Taken together, these findings suggest that the bottom-SEI mostly consists of lithium silicates, with some Li_xSi and trace residual SiO_2 . Given the thin layers and the interfacial roughness, we cannot exclude some vertical stratification (e.g., layering) of these components. Some lateral phase heterogeneity or nanoscale separation of lithium silicates and Li_xSi is also possible. The presence of low ion conductivity Li_xSiO_y ²⁶ also explains our previous observations of low ion transport kinetics through the SEI.²⁸ Starting from 0.6 V, an additional SEI layer consisting of inorganic electrolyte decomposition products forms on top of the bottom-SEI layer, which is denoted the “top-SEI.” At 0.2 V, Li_xSiO_y is further lithiated and Li_2O is formed in the bottom-SEI.^{22,57} The formation of Li_2O in the Li_xSiO_y layer has also been observed by a previous depth-profiling XPS study.²² Consistent with XRR results, the further lithiation of Li_xSiO_y and the formation of Li_2O cause the electron density of the bottom-SEI layer to decrease. Both the top- and bottom-SEI layers are largely inorganic SEI. The electron density of the top-SEI layer ($0.7\text{--}0.8\text{e}/\text{\AA}^3$) is higher than that of the bottom-SEI layer ($0.4\text{--}0.5\text{e}/\text{\AA}^3$), consistent with the picture of LiF in the top-SEI and $\text{Li}_x\text{SiO}_y/\text{Li}_x\text{Si}/\text{Li}_2\text{O}$ in the bottom-SEI. A previous XPS study⁵⁶ with depth profiling has shown that LiF is formed on top of Li_xSiO_y and SiO_2 after 1 lithiation/delithiation cycle. The thicknesses of the top- and bottom-SEI layers, are about 1 nm and 4 nm, respectively. The latter is consistent with a 2–3 times (15 \AA before lithiation, 38 \AA after lithiation) expansion of the native oxide upon lithiation.⁴³ This similarity between the expansion expected for lithiation forming only inorganic products and our measurements suggests that the bottom- and top-SEI layers contain minimal amounts of organic compounds and that the oxygen from the electrolyte decomposition is not needed to explain the thickening on lithiation, which is only due to the reaction between Li and SiO_2 . Despite this agreement, we cannot completely rule out the possibility that there may be some small electrolyte decomposition contributing to the inorganic SEI. Furthermore, the inorganic SEI is well layered, consistent with a previous cryo-EM study for SEI on Li anode.³⁶ We note that the reported physical and chemical parameters of the SEI only hold for voltages greater than 0.2 V, i.e., above the Si lithiation plateau at 0.1 V. Our previous studies^{27,28} show that the SEI continues to evolve during the bulk Si lithiation process.

We observed that the onset of LiF is at about 0.6 V and begins only after the onset of the lithiation of the native oxide. This is intriguing because quantum chemical (QC) calculations predict the reduction potential of LiPF_6 between ~ 1.45 and 1.6 V versus Li^+/Li .^{66,67} We thus hypothesize that the lower reduction potential for native oxide-terminated Si wafers is a result of the presence of the oxide; specifically, its large electrical resistivity ($10^{14}\text{--}10^{17}\text{ \Omega}\cdot\text{cm}$)^{68,69} kinetically hinders electrochemical electrolyte decomposition because the oxide limits electron transport. Only when the native oxide begins to be lithiated, forming Li_xSiO_y at 0.7 V with much lower resistivity ($10^5\text{--}10^{10}\text{ \Omega}\cdot\text{cm}$ depending on composition^{70,71}) and most likely a high defect concentration further promoting electrical conductivity, can electrons reach the Li_xSiO_y -electrolyte interface and reduce the electrolyte to form LiF.^{72–74} This is consistent with the formation of LiF on top of Li_xSiO_y .

To test this hypothesis, we performed LSV at 0.1 mV/s in the Teflon cone cell^{44,45} utilizing n-type doped single crystalline Silicon carbide (SiC). SiC is electrochemically non-active, sufficiently conducting (0.02–0.1 $\Omega\cdot\text{cm}$), and the surface oxidation is limited.⁷⁵ These measurements are shown in Figure S6. Indeed, we observed a reduction peak at 1.5 V, which we attribute to the QC predicted decomposition of LiPF₆ to LiF. This is consistent with previous experimental evidence of the LiPF₆ reduction around 1.6 V^{76–78} and QC calculations.⁶⁷ While it has recently been shown that LiF formation also occurs as a result of the electrocatalytic transformation of HF impurities in LiPF₆-containing electrolytes at much higher potentials on metals (~ 2 V),²⁵ we believe that our LSV reduction peak at 1.5 V on SiC corresponds to electrochemical reduction of LiPF₆. This is rationalized by considering the different reactivity of SiC, as compared to metal surfaces, conceptually consistent with the different reactivity of graphene and metal surfaces shown in Strmcnik et al. (2018)²⁵. Finally, we note that there is consistency between the reduction peaks in our LSV experiments and our XRR and XPS that show the formation LiF near 0.6 V. This suggests that the LiF in the top-SEI is formed by an electrochemical process, rather than by thermal degradation, a reaction with water,^{79,80} or other chemical processes.

Thus, our observations suggest that the native oxide acts as a protective layer, expanding the electrochemical stability window of LiPF₆-containing electrolytes to lower voltages of about 0.7 V by preventing LiPF₆ electrochemical reduction. This further leads us to hypothesize that the bottom-SEI (lithiation of native oxide) nucleates near the Si/SiO₂ junction within the oxide (in contrast to the oxide/electrolyte junction), i.e., Li ions diffuse through the native oxide to this interface, rather than electrons to the SiO₂-electrolyte interface, and that the top-SEI (LiF from decomposition products of LiPF₆) nucleates at the Li_xSiO_y-electrolyte interface where electrons and LiPF₆ can meet once Li_xSiO_y is sufficiently electrically conductive. This is consistent with the findings of Ariel et al. (2005),⁸¹ reporting Li ion diffusion through thin SiO₂ layers.

From our quantitative electrochemical LSV measurements, we can calculate the total charge passed into both the organic and inorganic SEI for a given voltage range. Our structural data allow us to estimate the capacity that corresponds to the formation of organic SEI, which we cannot observe in our structural characterization. Here, we use the quantitative XRR thickness and compositional information from XPS to convert electron density to mass density for the bottom-SEI, top-SEI, and initial Li_xSi. Specifically, we assume that Li₄SiO₄ makes up most of the bottom-SEI, that LiF is the main component of the top-SEI, and that initial Li_xSi is mainly composed of Li_{0.25}Si. We then estimate the charge consumed in the formation process of the bottom-SEI, top-SEI, and initial Li_xSi (details in the Supplemental Information). It is worth noting that the organic SEI can be formed both chemically and electrochemically,^{82,83} and the estimate presented here corresponds only to the electrochemically formed organic SEI, under the assumption that all charge passed into the system that does not correspond to the formation of the initial Li_xSi and inorganic SEI corresponds to the formation of organic SEI. For this purpose, we performed galvanostatic electrochemistry at 10 $\mu\text{A}/\text{cm}^2$ (GC), LSV at 0.1 mV/s, and potential hold experiments (shown in Figure S7). We conclude that for GC, only negligible amounts of organic SEI are formed; under LSV conditions, the capacity corresponding to the organic SEI is about 2.4 $\mu\text{Ah}/\text{cm}^2$; in GC, with 2-hr potential holds at 0.7, 0.6, 0.5 and 0.4 V, the capacity corresponding to the organic SEI is 5.7 $\mu\text{Ah}/\text{cm}^2$, trending to increased capacities with increased holding times. Previous studies have shown that faster cycling rates, or lithiation without holding processes, lead to a thinner SEI.^{32,33} We infer from our results that this phenomenon originates in less electrochemically formed organic SEI.

Conclusion

In conclusion, we have unraveled the SEI formation mechanism on a native oxide-terminated (001)-oriented Si wafer anode from a 1 M LiPF₆/EC/DMC electrolyte. A major finding is that the inorganic SEI consists of two parts: a bottom-SEI, which forms near the Si/SiO₂ junction at 0.7 V, and a top-SEI, which forms at the bottom-SEI|electrolyte interface at 0.6 V. The bottom-SEI contains mostly Li_xSiO_y, consistent with the literature,^{23,55} and the top-SEI contains LiF. While the electrolyte reduction is expected to occur at much higher potentials around 1.6 V, this reaction is kinetically hindered by the presence of an electrically insulating surface oxide. These findings provide fundamental insights into differences in SEI growth on Si anodes with and without native oxide termination. In this context, it has been previously shown⁸⁴ that, under identical electrochemical conditions, a thicker SEI with higher roughness is formed on HF-etched Si surfaces (no oxide) than on Si electrodes covered with native oxide. Therefore, we suggest that the growth of a smooth Li_xSiO_y bottom-SEI layer, formed from the atomically smooth native oxide, results in a conformally grown, smooth, and thin inorganic top-SEI layer. This indicates a possible advantage for the preparation of artificial thin ion-conduction SEI templates on electrodes in general, in cases where a thin and smooth SEI is desired. In real batteries, all Si anode particles are inevitably covered with a native oxide layer. Therefore, our study is essential in understanding the reaction of native oxide and the top-SEI layer growth on Li_xSiO_y, yielding insight into the initial capacity losses during the first cycle as well as into limiting factors during fast cycling rates. We hypothesize that if a thin and smooth SEI layer is desirable, for example to promote homogeneous lithiation, then the presence of the native oxide or similar natural or artificial surface layers may be beneficial. However, the native oxide may be counterproductive if a fast ion-conduction SEI is desired as Li_xSiO_y typically exhibit low ion conductivities.

EXPERIMENTAL PROCEDURES

Electrochemical Measurements

For *in situ* XRR measurements, (001) Si electrodes were cycled using a half-cell configuration in an electrochemical cell specifically designed for synchrotron XRR measurements.^{27,28} For *ex situ* XPS measurements, the same cell was used in order to ensure consistency. This also provides an advantage for *ex situ* studies as no mechanical impacts are expected in the disassembly of an open cell. For *ex situ* XPS, the Si anodes were galvanostatically cycled at 50 μA/cm² to the pre-set potentials (0.8, 0.7, 0.6, 0.3, and 0.2 V) and then held at the potential for 2 h. For LSV measurements, a Teflon cone electrochemical cell was used.^{44,45}

The working electrode was a (001)-terminated n-type doped Si wafer with a resistivity of 0.001–0.005 Ω·cm. A 2 nm-thick Ti adhesive layer and 100 nm-thick Cu layer were evaporated on the back side of the Si wafer to ensure good electrical contact. Li metal was used as a counter/reference electrode. A 1 M LiPF₆ in 1:1 wt % ethylene carbonate (EC):dimethyl carbonate (DMC) (BASF, LP30) solution was utilized as the non-aqueous electrolyte. The cells were assembled in an argon (Ar) glovebox (O₂ < 0.3 ppm). For *in situ* XRR measurements, the cell was inserted into an airtight chamber in the glovebox and then mounted on the beamline diffractometer; helium gas was continuously flowed through the chamber during the experiment to drive out Ar gas and to protect the cell from air and moisture. For *ex situ* XPS experiments, the cell was cycled in the Ar glovebox. Samples were taken out of the cell in the Ar glovebox, rinsed twice in fresh DMC baths, dried in the glovebox, and placed in an airtight transfer vessel. The vessel was taken to the XPS instrument and pumped to vacuum. Therefore, the Si anodes were never exposed to ambient air. The

electrochemistry was controlled by a Bio-Logic SP200 or SP150 potentiostat. All voltages in this manuscript are reported with respect to the Li⁺/Li redox potential, i.e., E_{we} versus Li/Li⁺ (V).

In Situ XRR Measurements

XRR is a surface/interface-sensitive technique with sub-nanometer spatial and minute temporal resolution frequently used in thin-film characterization^{85–87} and solid-liquid interfacial studies.^{48,88–90} XRR measures the intensity fraction of a monochromatic X-ray beam that is specularly reflected from a surface as a function of incident angle α . In this setup, the reflected angle β is equal to α , yielding a surface normal scattering vector $q_z = 4\pi \cdot \sin\alpha/\lambda$, where λ is the X-ray wavelength. For a thin film of thickness d , the interference of X-rays reflected from the top and bottom of the film results in Kiessig-fringes⁹¹ with a period of $\Delta q_z = 2\pi/d$. The q -dependence of the XRR intensity is related to the surface normal electron density profile. Specific to our system, this methodology was used to characterize the physical parameters, such as thickness and density, of the SEI film on Si wafer anodes during its voltage-dependent growth. We constructed a physically meaningful electron density profile $\rho_e(z)$ by combining a certain number of layers from which we calculated the XRR intensities^{92–94}; each layer has a thickness d , electron density ρ , and roughness σ . The roughness describes diffuseness of the junctions between the two layers via an interfacial width between each layer. This is conveniently described by an error-function. In the fitting routine, d , ρ , and σ of each layer were varied until the $\rho_e(z)$ -derived XRR matched the experimentally measured XRR data.

XRR experiments were performed at SSRL BL 2–1 with an X-ray energy of 12 keV ($\lambda = 1.033 \text{ \AA}$). The measured q_z -range covered from 0 to 0.5 \AA^{-1} . Each XRR measurement took approximately 5 min. Because XRR is a non-destructive technique, and hard X-rays (12 keV) can transmit through several millimeters of electrolyte (with attenuation length $\approx 2.9 \text{ mm}$), XRR enabled us to measure the sample under electrochemical cycling conditions.

Ex Situ X-Ray Photoelectron Spectroscopy Measurements

XPS probes the binding energy of photoelectrons emitted in the photoelectric effect and thus the chemical composition and thickness of surface layers. Specific to laboratory XPS, the penetration depth of photoelectrons is typically 2–4 nm for inorganic materials and 4–10 nm for organic materials,⁹⁵ rendering XPS a surface-sensitive technique. Specific to our systems, we utilized this methodology to study the chemical composition of the SEI as a function of electrochemical potential.

XPS experiments were performed at the Stanford Nano Shared Facility (SNSF) using a PHI Versaprobe 1 Scanning XPS Microprobe. The X-ray source was Al K-alpha at 1486.6 eV. The pass energy was set to 23.5 eV. Charge neutralization was used. Peak shifts due to surface charging were compensated by normalizing to the Si 2p literature value and shifting the corresponding spectra. Initially, this was achieved by sputtering until only Si 2p signal was observed in the spectra. This yielded Si 2p peak positions within 0.2 eV of the literature value. Remaining shifts were then corrected with respect to the Si 2p literature value in the final spectra. XPS fitting was performed using a PHI MultiPak 9.8.0.19.

Computational Voltage Profiles and Phase Stability

To predict the thermodynamically stable phases that form as a result of lithiation of the native oxide and relate these result to our XRR, XPS, and LSV findings, we utilized FPC from the MP³⁹ database (<http://www.materialsproject.com>). This database

contains structural, electronic, and thermodynamic data for approximately 70,000 compounds (as of October 2017) calculated using the DFT-based Vienna Ab initio Simulation Package (VASP).^{96–98} The electrochemical stability of SiO₂ was calculated using the grand potential phase diagrams constructed using pymatgen.^{97,98} Grand potential phase diagrams were constructed using the Phase Diagram App to evaluate the stability of a material in equilibrium with an external environment. In our case, we identified the thermodynamic phase equilibria of SiO₂ with an open Li reservoir of Li chemical potential μ_{Li} . The given phase is stable within a certain range of μ_{Li} . The chemical potential of Li is converted to cell potential using the following relation:

$$\mu_{\text{Li}}(V) = \mu_{\text{Li}}^0 - e \cdot V, \quad (\text{Equation 1})$$

where μ^0 is the chemical potential of the Li metal, e is the unit charge, and V is the cell potential in reference to the Li metal. The computational scheme behind the Li grand potential phase diagram assumes thermodynamic phase equilibrium.

Additionally, the voltages of amorphous Li_xSiO₂ configurations were computed using a combination of *ab initio* molecular dynamics (AIMD) and density functional theory as implemented in VASP. Representative amorphous structures for $0 < x < 8$ were found through a melt-quench process in AIMD as outlined by Akyol et al. (2018).⁶⁰ The total energies of the amorphous states are continuous, hence the average formation energy of the representative amorphous configurations were fit to a function $E_F(x)$. The Li chemical potential was thus calculated according to the following equation⁹⁹:

$$\mu_{\text{Li}} = \frac{dE_F(x)}{dx} (1 - x) + E_F(x), \quad (\text{Equation 2})$$

where x is the fraction of Li with respect to Li_xSiO₂. The cell potential was calculated using Equation 1.

SUPPLEMENTAL INFORMATION

Supplemental Information includes seven figures and three tables and can be found with this article online at <https://doi.org/10.1016/j.joule.2018.12.013>.

ACKNOWLEDGMENTS

It is a pleasure to thank Oleg Borodin (U.S. Army Research Laboratory) for fruitful discussions that inspired part of the conclusions drawn in this report. We gratefully acknowledge Matthijs van den Berg and Christopher E.D. Chidsey (Stanford) for kindly providing the Teflon cone electrochemical cell, and Natalie R. Geise (Stanford/SLAC) for assistance with initial experiments using this cell. We thank Dr. Doug Van Campen (SLAC) for his assistance during the design and fabrication of the *in situ* XRR cell. The experimental work was partly supported by the Joint Center for Energy Storage Research (JCESR). Research carried out at Stanford Synchrotron Radiation Lightsource, SLAC National Accelerator Laboratory, is supported by the U.S. Department of Energy, Office of Science, Office of Basic Energy Sciences, under Contract No. DE-AC02-76SF00515. I.I.A., C.J., B.M., and T.P.D. acknowledge support from the U.S. Department of Energy, Office of Basic Energy Sciences, Division of Materials Sciences and Engineering at the SLAC and Stanford for theoretical analysis. Part of this work was performed at the Stanford Nano Shared Facilities (SNSF), supported by the National Science Foundation under award ECCS-1542152. Additionally, this work was collaboratively funded by the Battery Materials Research (BMR) program, under the Assistant Secretary for Energy Efficiency and Renewable Energy, Office of Vehicle Technologies of the U.S. Department of Energy, Contract No. DE-AC02-05CH11231. This research also used resources of the Materials

Project, as funded by the U.S. Department of Energy, Office of Science, Office of Basic Energy Sciences, Materials Sciences and Engineering Division, under Contract No. DE-AC-02-05-CH11231; Materials Project program KC23MP and the National Energy Research Scientific Computing Center, a U.S. Department of Energy Office of Science User Facility operated under Contract No. DE-AC02-05CH11231.

AUTHOR CONTRIBUTIONS

C.C., H.-G.S., and M.F.T. conceived the idea and designed the project. C.C., I.I.A., B.S., and H.-G.S. performed the experiments and analyzed the data. I.I.A. and E.S. performed first principles calculations, utilized the Materials Project, and discussed the results with C.C., C.J., B.M., T.P.D., K.A.P., H.-G.S., and M.F.T. C.C., I.I.A., E.S., K.A.P., H.-G.S., and M.F.T. co-wrote the manuscript. All authors discussed the results and contributed to the manuscript.

DECLARATION OF INTERESTS

The authors declare no competing interests.

Received: September 4, 2018

Revised: November 1, 2018

Accepted: December 10, 2018

Published: January 17, 2019

REFERENCES

1. Chu, S., Cui, Y., and Liu, N. (2017). The path towards sustainable energy. *Nat. Mater.* **16**, 16–22.
2. Obama, B. (2017). The irreversible momentum of clean energy. *Science* **355**, 126–129.
3. Ashuri, M., He, Q., and Shaw, L.L. (2016). Silicon as a potential anode material for Li-ion batteries: Where size, geometry and structure matter. *Nanoscale* **8**, 74–103.
4. Jin, Y., Zhu, B., Lu, Z., Liu, N., and Zhu, J. (2017). Challenges and recent progress in the development of Si anodes for lithium-ion battery. *Adv. Energy Mater.* **7**, 1700715.
5. Zuo, X., Zhu, J., Müller-Buschbaum, P., and Cheng, Y.-J. (2017). Silicon based lithium-ion battery anodes: A chronicle perspective review. *Nano Energy* **31**, 113–143.
6. Zhao, J., Zhou, G., Yan, K., Xie, J., Li, Y., Liao, L., Jin, Y., Liu, K., Hsu, P.C., Wang, J., et al. (2017). Air-stable and freestanding lithium alloy/graphene foil as an alternative to lithium metal anodes. *Nat. Nanotechnol.* **12**, 993–999.
7. Li, J., and Dahn, J.R. (2007). An in situ X-ray diffraction study of the reaction of Li with Crystalline Si. *J. Electrochem. Soc.* **154**, A156.
8. Kganyago, K.R., and Ngoepe, P.E. (2003). Structural and electronic properties of lithium intercalated graphite LiC₆. *Phys. Rev. B* **68**, 205111.
9. Chan, C.K., Peng, H., Liu, G., McIlwrath, K., Zhang, X.F., Huggins, R.A., and Cui, Y. (2008). High-performance lithium battery anodes using silicon nanowires. *Nat. Nanotechnol.* **3**, 31–35.
10. Beaulieu, L.Y., Eberman, K.W., Turner, R.L., Krause, L.J., and Dahn, J.R. (2001). Colossal reversible volume changes in lithium alloys. *Electrochem. Solid State Lett.* **4**, A137.
11. Chew, H.B., Hou, B., Wang, X., and Xia, S. (2014). Cracking mechanisms in lithiated silicon thin film electrodes. *Int. J. Solids Struct.* **51**, 4176–4187.
12. Liu, X.H., Zhong, L., Huang, S., Mao, S.X., Zhu, T., and Huang, J.Y. (2012). Size-dependent fracture of silicon nanoparticles during lithiation. *ACS Nano* **6**, 1522–1531.
13. Maranchi, J.P., Hepp, A.F., Evans, A.G., Nuhfer, N.T., and Kumta, P.N. (2006). Interfacial properties of the a-Si/Cu: active-inactive thin-film anode system for lithium-ion batteries. *J. Electrochem. Soc.* **153**, A1246.
14. Dupré, N., Moreau, P., De Vito, E., Quazuguel, L., Boniface, M., Bordes, A., Rudisch, C., Bayle-Guillemaud, P., and Guyomard, D. (2016). Multiprobe study of the solid electrolyte interphase on silicon-based electrodes in full-cell configuration. *Chem. Mater.* **28**, 2557–2572.
15. Wang, A., Kadam, S., Li, H., Shi, S., and Qi, Y. (2018). Review on modeling of the anode solid electrolyte interphase (SEI) for lithium-ion batteries. *NPJ Comput. Mater.* **4**.
16. Peled, E., and Menkin, S. (2017). Review—SEI: past, present and future. *J. Electrochem. Soc.* **164**, A1703–A1719.
17. Tripathi, A.M., Su, W.N., and Hwang, B.J. (2018). In situ analytical techniques for battery interface analysis. *Chem. Soc. Rev.* **47**, 736–851.
18. Chan, C.K., Ruffo, R., Hong, S.S., and Cui, Y. (2009). Surface chemistry and morphology of the solid electrolyte interphase on silicon nanowire lithium-ion battery anodes. *J. Power Sources* **189**, 1132–1140.
19. Fears, T.M., Doucet, M., Browning, J.F., Baldwin, J.K.S., Winiarz, J.G., Kaiser, H., Taub, H., Sacci, R.L., and Veith, G.M. (2016). Evaluating the solid electrolyte interphase formed on silicon electrodes: a comparison of ex situ X-ray photoelectron spectroscopy and in situ neutron reflectometry. *Phys. Chem. Chem. Phys.* **18**, 13927–13940.
20. Fears, T.M., Sacci, R.L., Winiarz, J.G., Kaiser, H., Taub, H., and Veith, G.M. (2015). A study of perfluorocarboxylate ester solvents for lithium ion battery electrolytes. *J. Power Sources* **299**, 434–442.
21. Guo, B., Shu, J., Wang, Z., Yang, H., Shi, L., Liu, Y., and Chen, L. (2008). Electrochemical reduction of nano-SiO₂ in hard carbon as anode material for lithium ion batteries. *Electrochem. Commun.* **10**, 1876–1878.
22. Philippe, B., Dedryvère, R., Allouche, J., Lindgren, F., Gorgoi, M., Rensmo, H., Gonbeau, D., and Edström, K. (2012). Nanosilicon electrodes for lithium-ion batteries: Interfacial mechanisms studied by hard and soft X-ray photoelectron spectroscopy. *Chem. Mater.* **24**, 1107–1115.
23. Philippe, B., Dedryvère, R., Gorgoi, M., Rensmo, H., Gonbeau, D., and Edström, K. (2013). Improved performances of nanosilicon electrodes using the salt LiFSI: a photoelectron spectroscopy study. *J. Am. Chem. Soc.* **135**, 9829–9842.
24. Sun, Q., Zhang, B., and Fu, Z.-W. (2008). Lithium electrochemistry of SiO₂ thin film electrode for lithium-ion batteries. *Appl. Surf. Sci.* **254**, 3774–3779.
25. Strmcnik, D., Castelli, I.E., Connell, J.G., Haering, D., Zorko, M., Martins, P., Lopes, P.P., Genorio, B., Østergaard, T., Gasteiger, H.A.,

- et al. (2018). Electrocatalytic transformation of HF impurity to H₂ and LiF in lithium-ion batteries. *Nat. Catal.* 1, 255–262.
26. Deng, Y., Eames, C., Chotard, J.N., Lalère, F., Seznec, V., Emge, S., Pecher, O., Grey, C.P., Masquelier, C., and Islam, M.S. (2015). Structural and mechanistic insights into fast lithium-ion conduction in Li₄SiO₄–Li₃PO₄ solid electrolytes. *J. Am. Chem. Soc.* 137, 9136–9145.
27. Cao, C., Steinrück, H.G., Shyam, B., Stone, K.H., and Toney, M.F. (2016). In situ study of silicon electrode lithiation with X-ray reflectivity. *Nano Lett.* 16, 7394–7401.
28. Cao, C., Steinrück, H.G., Shyam, B., and Toney, M.F. (2017). The atomic scale electrochemical lithiation and delithiation process of silicon. *Adv. Mater. Interfaces* 4, 1700771.
29. Cresce, Av, Russell, S.M., Baker, D.R., Gaskell, K.J., and Xu, K. (2014). In situ and quantitative characterization of solid electrolyte interphases. *Nano Lett.* 14, 1405–1412.
30. Winter, M. (2009). The solid electrolyte interphase – The most important and the least understood solid electrolyte in rechargeable Li batteries. *Z. Physikalische Chem.* 223, 1395–1406.
31. Xu, K. (2014). Electrolytes and interphases in Li-ion batteries and beyond. *Chem. Rev.* 114, 11503–11618.
32. Tokranov, A., Kumar, R., Li, C., Minne, S., Xiao, X., and Sheldon, B.W. (2016). Control and optimization of the electrochemical and mechanical properties of the solid electrolyte interphase on silicon electrodes in lithium ion batteries. *Adv. Energy Mater.* 6, 1502302.
33. Tokranov, A., Sheldon, B.W., Li, C., Minne, S., and Xiao, X. (2014). In situ atomic force microscopy study of initial solid electrolyte interphase formation on silicon electrodes for Li-ion batteries. *ACS Appl. Mater. Interfaces* 6, 6672–6686.
34. Gür, T.M. (2018). Review of electrical energy storage technologies, materials and systems: Challenges and prospects for large-scale grid storage. *Energy Environ. Sci.* 11, 2696–2767.
35. Xiong, S., Diao, Y., Hong, X., Chen, Y., and Xie, K. (2014). Characterization of solid electrolyte interphase on lithium electrodes cycled in ether-based electrolytes for lithium batteries. *J. Electroanal. Chem.* 719, 122–126.
36. Li, Y., Li, Y., Pei, A., Yan, K., Sun, Y., Wu, C.-L., Joubert, L.-M., Chin, R., Koh, A.L., Yu, Y., et al. (2017). Atomic structure of sensitive battery materials and interfaces revealed by cryo-electron microscopy. *Science* 358, 506–510.
37. Lee, J.T., Nitta, N., Benson, J., Magasinski, A., Fuller, T.F., and Yushin, G. (2013). Comparative study of the solid electrolyte interphase on graphite in full Li-ion battery cells using X-ray photoelectron spectroscopy, secondary ion mass spectrometry, and electron microscopy. *Carbon* 52, 388–397.
38. Abate, I.L., Thompson, L.E., Kim, H.C., and Aetukuri, N.B. (2016). Robust NaO₂ electrochemistry in aprotic Na-O₂ batteries employing ethereal electrolytes with a protic additive. *J. Phys. Chem. Lett.* 7, 2164–2169.
39. Jain, A., Ong, S.P., Hautier, G., Chen, W., Richards, W.D., Dacek, S., Cholia, S., Gunter, D., Skinner, D., Ceder, G., et al. (2013). Commentary: the Materials Project: a materials genome approach to accelerating materials innovation. *APL Mater.* 1, 011002.
40. Steinrück, H.-G., Schiener, A., Schindler, T., Will, J., Magerl, A., Kononov, O., Li Destri, G., Seeck, O.H., Mezger, M., Haddad, J., et al. (2014). Nanoscale structure of Si/SiO₂/organics interfaces. *ACS Nano* 8, 12676–12681.
41. Heinrich, F., Ng, T., Vanderah, D.J., Shekhar, P., Mihailescu, M., Nanda, H., and Lösche, M. (2009). A new lipid anchor for sparsely tethered bilayer lipid membranes. *Langmuir* 25, 4219–4229.
42. Khassanov, A., Steinrück, H.G., Schmaltz, T., Magerl, A., and Halik, M. (2015). Structural investigations of self-assembled monolayers for organic electronics: results from X-ray reflectivity. *Acc. Chem. Res.* 48, 1901–1908.
43. Zhang, Y., Li, Y., Wang, Z., and Zhao, K. (2014). Lithiation of SiO₂ in Li-ion batteries: In situ transmission electron microscopy experiments and theoretical studies. *Nano Lett.* 14, 7161–7170.
44. Chen, Y.W., Prange, J.D., Dühnen, S., Park, Y., Gunji, M., Chidsey, C.E.D., and McIntyre, P.C. (2011). Atomic layer-deposited tunnel oxide stabilizes silicon photoanodes for water oxidation. *Nat. Mater.* 10, 539–544.
45. Satterthwaite, P.F., Scheuermann, A.G., Hurley, P.K., Chidsey, C.E.D., and McIntyre, P.C. (2016). Engineering interfacial silicon dioxide for improved metal-insulator-semiconductor silicon photoanode water splitting performance. *ACS Appl. Mater. Interfaces* 8, 13140–13149.
46. Wagner, C.D., Naumkin, A.V., Kraut-Vass, A., Allison, J.W., Powell, C.J., and Rumble, J.R., Jr. (2003). NIST Standard Reference Database 20 (Version). <https://srdata.nist.gov/xps/>.
47. Kibel, M.H., and Leech, P.W. (1996). X-ray photoelectron spectroscopy study of optical waveguide glasses. *Surf. Interface Anal.* 24, 605–610.
48. Horowitz, Y., Steinrück, H.G., Han, H.L., Cao, C., Abate, I.L., Tsao, Y., Toney, M.F., and Somorjai, G.A. (2018). Fluoroethylene carbonate induces ordered electrolyte interface on silicon and sapphire surfaces as revealed by sum frequency generation vibrational spectroscopy and X-ray reflectivity. *Nano Lett.* 18, 2105–2111.
49. Radvanyi, E., De Vito, E., Porcher, W., and Jouanneau Si Larbi, S. (2014). An XPS/AES comparative study of the surface behaviour of nano-silicon anodes for Li-ion batteries. *J. Anal. At. Spectrom.* 29, 1120–1131.
50. Lu, P., Li, C., Schneider, E.W., and Harris, S.J. (2014). Chemistry, impedance, and morphology evolution in solid electrolyte interphase films during formation in lithium ion batteries. *J. Phys. Chem. C* 118, 896–903.
51. Tasaki, K., Goldberg, A., Lian, J.-J., Walker, M., Timmons, A., and Harris, S.J. (2009). Solubility of lithium salts formed on the lithium-ion battery negative electrode surface in organic solvents. *J. Electrochem. Soc.* 156, A1019.
52. Sim, S., Oh, P., Park, S., and Cho, J. (2013). Critical thickness of SiO₂ coating layer on core@shell bulk@nanowire Si anode materials for Li-ion batteries. *Adv. Mater.* 25, 4498–4503.
53. Yan, N., Wang, F., Zhong, H., Li, Y., Wang, Y., Hu, L., and Chen, Q. (2013). Hollow porous SiO₂ nanocubes towards high-performance anodes for lithium-ion batteries. *Sci. Rep.* 3, 1568.
54. Favors, Z., Wang, W., Bay, H.H., George, A., Ozkan, M., and Ozkan, C.S. (2014). Stable cycling of SiO₂ Nanotubes as high-performance anodes for lithium-ion batteries. *Sci. Rep.* 4, 4605.
55. Schroder, K.W., Celio, H., Webb, L.J., and Stevenson, K.J. (2012). Examining solid electrolyte interphase formation on crystalline silicon electrodes: Influence of electrochemical preparation and ambient exposure conditions. *J. Phys. Chem. C* 116, 19737–19747.
56. Young, B.T., Heskett, D.R., Nguyen, C.C., Nie, M., Wocik, J.C., and Lucht, B.L. (2015). Hard X-ray photoelectron spectroscopy (HAXPES) investigation of the silicon solid electrolyte interphase (SEI) in lithium-ion batteries. *ACS Appl. Mater. Interfaces* 7, 20004–20011.
57. Coyle, J., Apblett, C., Brumbach, M., Ohlhausen, J., and Stoldt, C. (2017). Structural and compositional characterization of RF magnetron cosputtered lithium silicate films: from Li₂Si₂O₅ to lithium-rich Li₈SiO₆. *J. Vac. Sci. Technol. A* 35, 061509.
58. Ferraresi, G., Czornomaz, L., Villeveille, C., Novák, P., and El Kazzi, M. (2016). Elucidating the surface reactions of an Amorphous Si thin film as a model electrode for Li-Ion batteries. *ACS Appl. Mater. Interfaces* 8, 29791–29798.
59. Kim, S.-Y., and Qi, Y. (2014). Property evolution of Al₂O₃Coated and Uncoated Si electrodes: A first principles investigation. *J. Electrochem. Soc.* 161, F3137–F3143.
60. Aykol, M., and Persson, K.A. (2018). Oxidation protection with amorphous surface oxides: Thermodynamic insights from ab initio simulations on aluminum. *ACS Appl. Mater. Interfaces* 10, 3039–3045.
61. Sun, W., Dacek, S.T., Ong, S.P., Hautier, G., Jain, A., Richards, W.D., Gamst, A.C., Persson, K.A., and Ceder, G. (2016). The thermodynamic scale of inorganic crystalline metastability. *Sci. Adv.* 2, e1600225.
62. Morita, M., Ohmi, T., Hasegawa, E., Kawakami, M., and Ohwada, M. (1990). Growth of native oxide on a silicon surface. *J. Appl. Phys.* 68, 1272–1281.
63. Vogl, U.S., Lux, S.F., Das, P., Weber, A., Placke, T., Kostecki, R., and Winter, M. (2015). The mechanism of SEI formation on single crystal Si(100), Si(110) and Si(111) electrodes. *J. Electrochem. Soc.* 162, A2281–A2288.
64. Vogl, U.S., Lux, S.F., Crumlin, E.J., Liu, Z., Terborg, L., Winter, M., and Kostecki, R. (2015). The mechanism of SEI formation on a single crystal Si(100) electrode. *J. Electrochem. Soc.* 162, A603–A607.
65. Arreaga-Salas, D.E., Sra, A.K., Roodenko, K., Chabal, Y.J., and Hinkle, C.L. (2012). Progression of solid electrolyte interphase formation on hydrogenated amorphous silicon

- anodes for lithium-ion batteries. *J. Phys. Chem. C* **116**, 9072–9077.
66. Leung, K. (2015). Predicting the voltage dependence of interfacial electrochemical processes at lithium-intercalated graphite edge planes. *Phys. Chem. Chem. Phys.* **17**, 1637–1643.
67. Borodin, O., Ren, X., Vatamanu, J., von Wald Cresce, A., Knap, J., and Xu, K. (2017). Modeling insight into battery electrolyte electrochemical stability and interfacial structure. *Acc. Chem. Res.* **50**, 2886–2894.
68. El-Kareh, B. (2012). *Fundamentals of Semiconductor Processing Technology* (Springer Science and Business Media).
69. Sze, S.M., and Ng, K.K. (2006). *Physics of Semiconductor Devices* (John Wiley & Sons).
70. Yoshiyagawa, M., and Tomozawa, M. (1982). Electrical properties of rapidly quenched lithium-silicate glasses. *J. Phys. Colloq.* **43**, C9-411-C9-414.
71. Charles, R.J. (1963). Some structural and electrical properties of lithium silicate glasses. *J. Am. Ceram. Soc.* **46**, 235–238.
72. Chattopadhyay, S., Lipson, A.L., Karmel, H.J., Emery, J.D., Fister, T.T., Fenter, P.A., Hersam, M.C., and Bedzyk, M.J. (2012). In situ x-ray study of the solid electrolyte interphase (SEI) formation on graphene as a model Li-ion battery anode. *Chem. Mater.* **24**, 3038–3043.
73. Kanamura, K., Tamura, H., and Takehara, Z.-i (1992). XPS analysis of a lithium surface immersed in propylene carbonate solution containing various salts. *J. Electroanal. Chem.* **333**, 127–142.
74. Yan, J., Xia, B.-J., Su, Y.-C., Zhou, X.-Z., Zhang, J., and Zhang, X.-G. (2008). Phenomenologically modeling the formation and evolution of the solid electrolyte interface on the graphite electrode for lithium-ion batteries. *Electrochim. Acta* **53**, 7069–7078.
75. Öneby, C., and Pantano, C.G. (1997). Silicon oxycarbide formation on SiC surfaces and at the SiC/SiO₂ interface. *J. Vac. Sci. Technol. A Vac. Surf. Films* **15**, 1597–1602.
76. Delp, S.A., Borodin, O., Olguin, M., Eisner, C.G., Allen, J.L., and Jow, T.R. (2016). Importance of reduction and oxidation stability of high voltage electrolytes and additives. *Electrochim. Acta* **209**, 498–510.
77. Nie, M., Abraham, D.P., Seo, D.M., Chen, Y., Bose, A., and Lucht, B.L. (2013). Role of solution structure in solid electrolyte interphase formation on graphite with LiPF₆ in propylene carbonate. *J. Phys. Chem. C* **117**, 25381–25389.
78. Kawaguchi, T., Shimada, K., Ichitsubo, T., Yagi, S., and Matsubara, E. (2014). Surface-layer formation by reductive decomposition of LiPF₆ at relatively high potentials on negative electrodes in lithium ion batteries and its suppression. *J. Power Sources* **271**, 431–436.
79. Lux, S.F., Lucas, I.T., Pollak, E., Passerini, S., Winter, M., and Kostecki, R. (2012). The mechanism of HF formation in LiPF₆ based organic carbonate electrolytes. *Electrochem. Commun.* **14**, 47–50.
80. Plakhotnyk, A.V., Ernst, L., and Schmutzler, R. (2005). Hydrolysis in the system LiPF₆—Propylene carbonate—Dimethyl carbonate—H₂O. *J. Fluor. Chem.* **126**, 27–31.
81. Ariel, N., Ceder, G., Sadoway, D.R., and Fitzgerald, E.A. (2005). Electrochemically controlled transport of lithium through ultrathin SiO₂. *J. Appl. Phys.* **98**, 023516-023516-7.
82. Michan, A.L., Leskes, M., and Grey, C.P. (2016). Voltage dependent solid electrolyte interphase formation in silicon electrodes: Monitoring the formation of organic decomposition products. *Chem. Mater.* **28**, 385–398.
83. Ganesh, P., Kent, P.R.C., and Jiang, D.-E. (2012). Solid–electrolyte interphase formation and electrolyte reduction at Li-ion battery graphite anodes: insights from first-principles molecular dynamics. *J. Phys. Chem. C* **116**, 24476–24481.
84. Schroder, K.W., Dylla, A.G., Harris, S.J., Webb, L.J., and Stevenson, K.J. (2014). Role of surface oxides in the formation of solid–electrolyte interphases at silicon electrodes for lithium-ion batteries. *ACS Appl. Mater. Interfaces* **6**, 21510–21524.
85. Daillant, J., and Gibaud, A. (2008). *X-Ray and Neutron Reflectivity: Principles and Applications*, 770 (Springer).
86. Pershan, P.S., and Schlossman, M. (2012). *Liquid Surfaces and Interfaces: Synchrotron X-Ray Methods* (Cambridge University Press).
87. Tolan, M. (1999). *X-Ray Scattering from Soft-Matter Thin Films* (Springer).
88. Steinrück, H.-G., Cao, C., Tsao, Y., Takacs, C.J., Konovalov, O., Vatamanu, J., Borodin, O., and Toney, M.F. (2018). The nanoscale structure of the electrolyte–metal oxide interface. *Energy Environ. Sci.* **11**, 594–602.
89. Mezger, M., Schröder, H., Reichert, H., Schramm, S., Okasinski, J.S., Schöder, S., Honkimäki, V., Deutsch, M., Ocko, B.M., and Ralston, J. (2008). Molecular layering of fluorinated ionic liquids at a charged sapphire (0001) surface. *Science* **322**, 424–428.
90. Lee, S.S., Fenter, P., Nagy, K.L., and Sturchio, N.C. (2017). Real-time observation of cation exchange kinetics and dynamics at the muscovite–water interface. *Nat. Commun.* **8**, 15826.
91. Kiessig, H. (1931). Interferenz von Röntgenstrahlen an dünnen Schichten. *Ann. Phys.* **402**, 769–788.
92. Abeles, F. (1950). Investigations on the propagation of sinusoidal electromagnetic waves in stratified media. Application to thin films. *Ann. Phys. (Paris)* **5**, 596–640.
93. Als-Nielsen, J., and McMorrow, D. (2001). *Elements of Modern X-Ray Physics* (Wiley).
94. Parratt, L.G. (1954). Surface studies of solids by total reflection of x-rays. *Phys. Rev.* **95**, 359–369.
95. Powell, C.J., and Jablonski, A. (2000). NIST Electron Inelastic-Mean-Free-Path Database, [1.1. Version] 71.
96. Kresse, G., and Furthmüller, J. (1996). Efficient iterative schemes for ab initio total-energy calculations using a plane-wave basis set. *Phys. Rev. B* **54**, 11169–11186.
97. Ong, S.P., Jain, A., Hautier, G., Kang, B., and Ceder, G. (2010). Thermal stabilities of delithiated olivine MPO₄ (M=Fe, Mn) cathodes investigated using first principles calculations. *Electrochem. Commun.* **12**, 427–430.
98. Ong, S.P., Wang, L., Kang, B., and Ceder, G. (2008). Li–Fe–P–O 2 phase diagram from first principles calculations. *Chem. Mater.* **20**, 1798–1807.
99. Aydinol, M.K., Kohan, A.F., Ceder, G., Cho, K., and Joannopoulos, J. (1997). Ab initio study of lithium intercalation in metal oxides and metal dichalcogenides. *Phys. Rev. B* **56**, 1354–1365.